



Article

Mapping Alteration Minerals Using ZY-1 02D Hyperspectral Remote Sensing Data in Coalbed Methane Enrichment Areas

Li Chen, Xinxin Sui *, Rongyuan Liu, Hong Chen, Yu Li, Xian Zhang and Haomin Chen

China Aero Geophysical Survey and Remote Sensing Center for Natural Resources, Beijing 100083, China; cli_a@mail.cgs.gov.cn (L.C.); liurongyuan@mail.cgs.gov.cn (R.L.); chong@mail.cgs.gov.cn (H.C.); liyu@mail.cgs.gov.cn (Y.L.); zhangxian@mail.cgs.gov.cn (X.Z.); chenhaomin@mail.cgs.gov.cn (H.C.)

* Correspondence: suixinxin@mail.cgs.gov.cn

Abstract: As a clean energy resource, coalbed methane (CBM) is an important industry in China's dual-carbon strategic planning. Despite the immense potential of CBM resources in China, the current exploration level remains low due to outdated survey technology, impeding large-scale exploration and development. This study investigates the application of hyperspectral data in CBM enrichment areas, specifically focusing on the extraction of alteration minerals in the Hudi coal mine area of the Qinshui Basin using ZY-1 02D and Hyperion hyperspectral data. The hyperspectral alteration mineral identification methods are summarized and analyzed. A method that combines spectral feature matching and diagnostic characteristic parameters is proposed for mineral extraction based on the spectral characteristics of different minerals. The extraction results are verified through field samples using X-ray diffraction analysis. Results show that (1) both ZY-1 02D and Hyperion hyperspectral data yield favorable extraction results for clay and carbonate minerals; (2) the overall accuracy of clay and carbonate minerals extraction is higher using ZY-1 02D data compared with Hyperion data, with accuracies of 81.67% and 79.03%, respectively; (3) the proposed method effectively extracts alteration minerals in CBM enrichment areas using hyperspectral data, thereby providing valuable technical support for the application of hyperspectral data.

Keywords: hyperspectral remote sensing; ZY-1-02D; Hyperion; alteration mineral; coalbed methane enrichment areas



Citation: Chen, L.; Sui, X.; Liu, R.; Chen, H.; Li, Y.; Zhang, X.; Chen, H. Mapping Alteration Minerals Using ZY-1 02D Hyperspectral Remote Sensing Data in Coalbed Methane Enrichment Areas. *Remote Sens.* **2023**, *15*, 3590. <https://doi.org/10.3390/rs15143590>

Academic Editor: Geert Verhoeven

Received: 27 June 2023

Revised: 7 July 2023

Accepted: 11 July 2023

Published: 18 July 2023



Copyright: © 2023 by the authors. Licensee MDPI, Basel, Switzerland. This article is an open access article distributed under the terms and conditions of the Creative Commons Attribution (CC BY) license (<https://creativecommons.org/licenses/by/4.0/>).

1. Introduction

In China's dual-carbon strategic planning, coalbed methane (CBM) has emerged as an important clean energy resource. More than 90% of CBM comprises methane (CH₄), along with other heavier hydrocarbons, such as CO₂, N₂, C₃H₈, C₄H₁₀, and others [1]. Nevertheless, methane remarkably contributes to the greenhouse effect, ozone layer depletion, global warming, and environmental damage. As the world's largest energy producer, China has strongly supported and developed the exploration and development of CBM enrichment areas [2]. However, traditional exploration methods for CBM enrichment areas mainly rely on ground drilling, seismic exploration, geophysical techniques, and geochemical surveys [3,4]. These methods suffer from exploration efficiency, limited scope, and the need for substantial human, financial, and material resources. In particular, exploration risks increase dramatically in mountainous areas. Efficient, economical, and accurate identification of CBM enrichment areas has become an urgent problem.

Satellite remote sensing technology possesses the capability to detect and analyze surface rock and mineral composition with precision [5–10]. Specifically, hyperspectral data provide high-resolution images for ground object classification and enable detailed analysis of the chemical composition of certain minerals [11–15]. In recent years, hyperspectral remote sensing technology has played an important role in mineral identification [16–18], geological mapping [19], alteration anomaly zoning [20,21], and prospecting prediction [22,23]. For example, mineral mapping has been conducted in the Eastern Tien Shan, Xinjiang, and

the Maherabad area in eastern Iran using HyMap data [24,25]. Fine mineral identification has been applied in Liuyuan, Gansu, and Cuprite, USA, using GF-5 hyperspectral imagery [26]. However, research on the hyperspectral characteristics of different alteration minerals in CBM enrichment areas is scarce. Studies have revealed that hydrocarbon microseepage phenomena exist in more than 85% of discovered oil and gas fields worldwide [4]. These phenomena subject the surface soil and rock to prolonged exposure to hydrocarbon substances, leading to alterations through various physical and chemical processes, including the enrichment of clay minerals, carbonate minerals, and iron minerals [27]. The application of hyperspectral remote sensing technology holds the potential to prospect CBM enrichment areas, effectively compensating for the limitations of traditional exploration methods and providing an important technical method for the efficient and rapid identification of CBM enrichment areas. While information about the abnormal alteration of minerals is rare and easily affected by external interference, the difficulty of identification of CBM enrichment areas has greatly increased.

The ZY-1 02D was successfully launched in China on 12 September 2019. It operates in a solar synchronous orbit with a ground coverage width of 60 km, an average orbital altitude of 778 km, and an inclination of 98.5° [28,29]. The satellite is equipped with a visible near-infrared camera and a hyperspectral camera (AHSI). The AHSI data provides a total of 166 visible near-infrared short-wave bands. This includes 76 visible near-infrared (VNIR) bands with a wavelength range of 395–1040 nm and a spectral resolution of 10 nm, and 90 short-wave infrared (SWIR) bands with a wavelength range of 1005–2501 nm and a spectral resolution of 20 nm [30,31]. At present, ZY1-02D hyperspectral data have been applied in land use classification and geological and mineral exploration [32,33].

ZY-1 02D hyperspectral data provide a basis for investigating the diagnostic spectral characteristics of alteration minerals in CBM enrichment areas. To solve the problems of tiny abnormal information extraction, the purpose of this study is to analyze the diagnostic spectral characteristics of different alteration minerals in CBM using ZY-1 02D hyperspectral data. This analysis aims to extract typical alteration minerals within the study area through a method that combines spectral feature matching and diagnostic characteristic parameters. Hyperion, the world's first successfully launched civilian satellite hyperspectral imaging spectrometer, is onboard the National Aeronautics and Space Administration Earth Observer-1 (EO-1) satellite [34,35]. The study demonstrates the capability of domestic data to extract alteration minerals through comparing the extraction results with Hyperion data and conducting field verification. This research provides valuable support for the identification of alteration minerals and the prediction of CBM enrichment areas.

2. Study Area and Data Sources

2.1. Study Area

Qinshui Basin, an important coal-bearing basin in China, is predominantly composed of anthracite and medium-high metamorphic bituminous coal. It boasts abundant coal resources, with a total reserves of approximately 2700×10^8 t [36]. The geological characteristics of this basin provide a favorable foundation for the formation of CBM reservoirs. The study area specifically encompasses the southeast margin of Qinshui Basin, located in Hudi Town, Qinshui County, Jincheng City, Shanxi Province [37]. The geographical extent of the study region spans from 112°30'E to 112°40'E and 35°35'N to 35°50'N, covering an total area of approximately 500 km² (Figure 1).

The study area is characterized by complex topography, featuring low mountains, hills, and distinct loess landform. It is situated within a sedimentary basin formed through the transformation and deformation of the Paleozoic Craton basin in North China. The stratigraphic sequence includes Ordovician (O), Carboniferous (C), Permian (P), Triassic (T), Paleogene (E), Neogene (N), and Quaternary (Q) formations, with a general trend of NNE and a dip angle of less than 10° in the study area [26]. The lithology consists of limestone, sandstone, siltstone, mudstone, sandy mudstone, and argillaceous sandstone. The structural complexity in the study area is relatively low, primarily characterized by

folds, with a limited occurrence of faults and no magmatic rock activity. The main coal-bearing strata consist of the Carboniferous Taiyuan Formation and the Permian Shanxi Formation, with coal seams found at depths of less than 800 m. The No. 3 coal seam of the Shanxi Formation and the No. 15 coal seam of the Taiyuan Formation are the primary coal seams being mined in the study area, renowned for their stable development and high gas content [37].

In CBM enrichment areas, the presence of hydrocarbon microseepage leads to widespread mineral alterations, such as clayization, carbonatization, and mineralization. Therefore, the diagnostic hyperspectral response characteristics of clay and carbonate minerals are considered indicative features for distinguishing and extracting alteration information in CBM enrichment areas using hyperspectral remote sensing techniques.

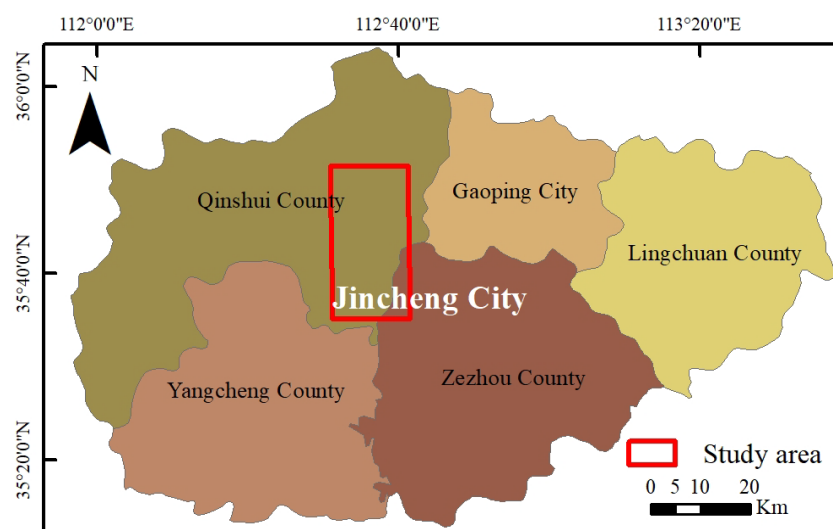


Figure 1. Location of the study area.

2.2. Data

2.2.1. Hyperspectral Remote Sensing Data

The ZY-1 02D is China's first independently developed civilian hyperspectral satellite. AHSI is the one of the important payloads onboard the ZY-1 02D satellite. The SWIR spectrum of AHSI data, in particular, exhibits excellent spectral features, making it well-suited for distinguishing the diagnostic spectral features of ground objects. The ZY-1 02D AHSI data used in this study were captured on 21 October 2020 and have no cloud coverage.

Hyperion data are highly suitable for extracting alteration minerals in CBM enrichment areas due to their most useful spectral features in the NIR and SWIR bands. The Hyperion image used for verification in this research was acquired on 6 October 2014, under cloud-free conditions. A comparison of specific parameters between the ZY-1 02D AHSI and EO-1 Hyperion is presented in Table 1.

Table 1. Comparison of specific parameters for the ZY-1 02D AHSI and EO-1 Hyperion.

Parameters	ZY-1 02D AHSI	EO-1 Hyperion
Average orbital altitude/km	778	705
Inclination/(°)	98.5	98.7
Width/km	60	7.5
Spatial resolution/m	30	30
Band number	166	242
Band range/nm	395–1040 (VNIR); 1005–2501 (SWIR)	356–1058 (VNIR); 852–2577 (SWIR)
Spectral resolution/nm	10 (VNIR); 20 (SWIR)	10

2.2.2. Field Sample Data

Abundant field data, including various types of rock and soil samples, were collected in the study area in October 2014 and 2017, corresponding to the image acquisition time to verify the extraction results from the hyperspectral remote sensing images. The field measured spectra of these samples were obtained using an Analytical Spectral Devices FieldSpec3 spectrometer on cloudless days between 10:00 and 14:00. During measurement, the probe was held perpendicular to the detection target to eliminate the effects of various interference factors. A standard white panel was used for calibration before each measurement, and the average of five measurements was used as the final spectral curve after applying Savitzky–Golay smooth filtering to remove noise. A total of 300 spectral curves were obtained from 60 field samples, covering a wavelength range of 350 nm to 2500 nm in the study area. An example of the spectral curves is shown in Figure 2. X-ray diffraction (XRD) analysis was performed on the field samples for further quantitative analysis.

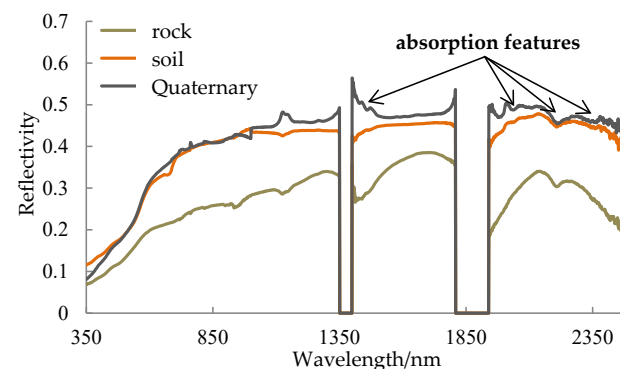


Figure 2. Field spectra curves of rock and soil.

3. Methods

This methodology includes the following four steps: theoretical basis, data preprocessing, alteration information extraction, and accuracy assessment. Firstly, the hydrocarbon microseepage theory was introduced, and diagnostic hyperspectral characteristics of alteration minerals, such as the typical clay and carbonate minerals, was analyzed. Secondly, data preprocessing was performed. Next, integrated extraction method of spectral feature matching and diagnostic characteristic parameters for alteration minerals was proposed. Finally, accuracy assessment was carried out. The technical flowchart is shown in Figure 3.

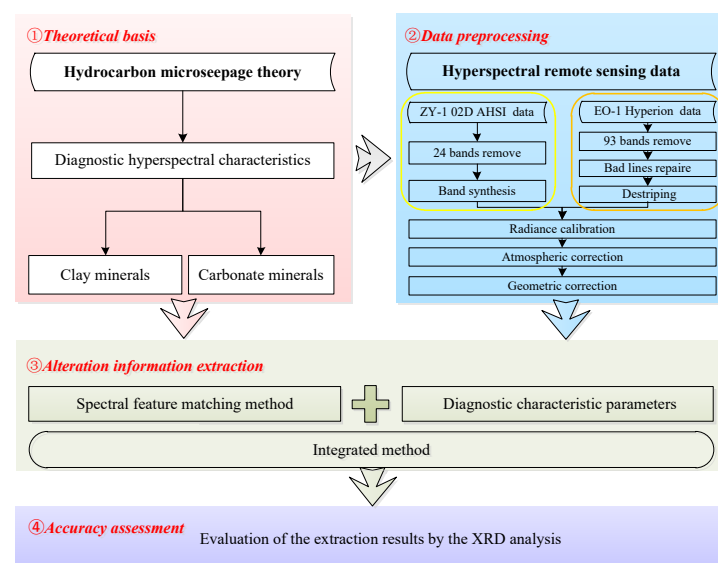


Figure 3. Technical flowchart of the methodology in this research.

3.1. Hydrocarbon Microseepage Theory and Diagnostic Hyperspectral Characteristics of Alteration Minerals

Hydrocarbon microseepage is a complex process that occurs in CBM enrichment areas. Under a specific temperature, pressure, and hydrodynamic conditions, CBM remains relatively stable. However, CBM undergoes diffusion and migration to the roof and floor when external conditions change. The double-pore structure of matrix pores and cracks in coal seams, along with the existence of fault structures, provides a channel for the migration of CBM, allowing it to penetrate the cap rock and reach the surface [38]. Prolonged hydrocarbon microseepage alters the surface redox environment and promotes the enrichment of altered minerals, such as ferrous iron mineralization, clayization, and carbonatization [39]. Hence, CBM enrichment areas can be identified using the diagnostic hyperspectral characteristics of alteration minerals based on hydrocarbon microseepage theory.

Different minerals exhibit distinctive diagnostic spectral characteristics. For instance, kaolinite, a clay mineral, displays a strong absorption feature at 2.2 μm in the SWIR region. Siderite, which is both a ferrous iron and carbonate mineral, exhibits diagnostic spectral characteristics at approximately 1.0–1.1 μm and 2.3 μm , respectively. The asymmetric diagnostic absorption feature at 2.3 μm is particularly important for the identification of carbonate minerals [40]. The spectral characteristics of typical clay and carbonate minerals provided by the USGS_MIN spectral library are shown in Figure 4.

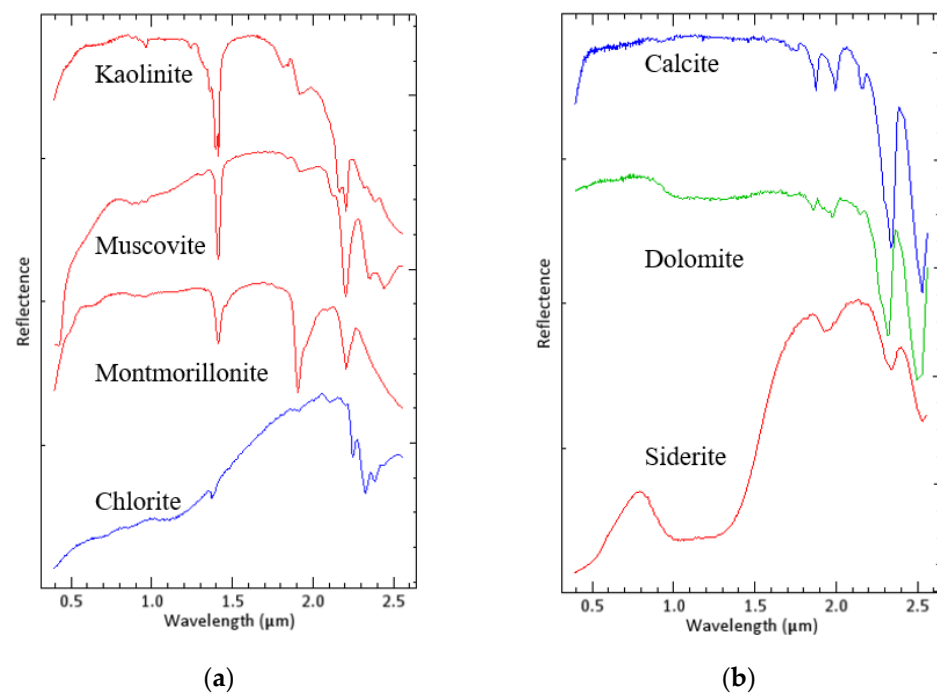


Figure 4. Spectral characteristics of typical clay and carbonate minerals in the USGS_MIN spectral library. (a) Clay minerals; (b) Carbonate minerals.

3.1.1. Clay Minerals

Clay minerals are mainly silicate minerals containing aluminum, iron, and magnesium, along with water. The long-term microseepage of hydrocarbons and hydrogen sulfide leads to the alteration of feldspar minerals into clay minerals, enriching them on the surface redox environment [41]. Typical clay minerals include kaolinite, montmorillonite, chlorite, and muscovite. The main absorption characteristics of clay minerals are observed around 1.4, 1.9, and 2.2–2.3 μm . However, each mineral possesses its unique absorption characteristics, as shown in Table 2.

Table 2. Spectral characteristics of typical clay minerals (μm).

Name	Wavelength of Absorption	Wavelength of Reflection
Kaolinite	1.403, 1.915, 2.205	0.720–1.263, 1.513–1.780
Muscovite	1.403, 1.925, 2.205	0.933–1.343, 1.478–2.075
Montmorillonite	1.418, 1.905, 2.225	0.785–1.308, 1.570–1.825
Chlorite	1.388, 1.985, 2.315	1.825, 2.135

The spectral characteristics of kaolinite and muscovite are similar, showing strong absorption spectra at 1.4 and 2.2 μm , along with weak absorption spectra at 1.9 μm . Montmorillonite exhibits adsorption depths comparable to kaolinite at 1.4 and 2.2 μm , while demonstrating strong absorption at 1.9 μm . However, the spectral characteristics of chlorite are relatively different from the aforementioned three types. Chlorite exhibits absorption at 2.3 μm , but does not show obvious adsorption at 1.4 and 1.9 μm .

3.1.2. Carbonate Minerals

The microseepage of hydrocarbons reaching the surface, combined with action of oxygen, leads to the production of carbon dioxide. In a long-term acidic environment, carbonate minerals, such as calcite, dolomite, and siderite, become enriched on the surface due to the precipitation of various metal ions, forming carbonate mineralization halos [42]. The spectral characteristics of carbonate are mainly between 1.7–2.5 μm , with at least 5 absorption features observed, particularly at 2.3 and 2.5 μm , which serve as typical bands for identifying carbonate minerals, as shown in Table 3.

Table 3. Spectral characteristics of typical carbonate minerals (μm).

Name	Wavelength of Absorption		Wavelength of Reflection	
	Weak Absorption	Strong Absorption	Weak Reflection	Strong Reflection
Calcite	1.875, 1.995, 2.155	2.335, 2.528	1.915, 2.065, 2.185	2.386
Dolomite	1.855, 1.985	2.315, 2.528	1.885, 2.025	2.375
Siderite	1.945	2.335, 2.528	1.855, 2.145	2.400

The absorption characteristics of calcite exhibit strong absorption near 2.335 and 2.528 μm , and weak absorption near 1.875, 1.995, and 2.155 μm . Both dolomite and siderite display consistent strong adsorption after 2.3 and 2.5 μm . However, siderite exhibits weak absorption characteristics specifically at 1.945 μm . In summary, the absorption characteristics of carbonate minerals are mainly observed in the range of 2.31–2.35 μm and 2.52 μm . The content of carbonate minerals demonstrates a strong correlation with the absorption depth, absorption area, and symmetry of the abovementioned spectral characteristics. Therefore, the identification and extraction of carbonate minerals can be achieved through considering the three absorption feature parameters of the characteristic spectrum.

3.2. Data Preprocessing

The main data preprocessing steps for ZY-1 02D AHSI data are as follows: (1) band synthesis, (2) radiance calibration, (3) atmospheric correction, and (4) geometric correction [43]. The VNIR and SWIR bands were combined to create a spectral coverage ranging from 395 nm to 2 501 nm. Three overlapping bands (band 77–79) in the near-infrared range and 21 noise bands (band 97–103, 125–133, 137, 163–166) were eliminated, resulting in a total of 142 bands. Radiance calibration was performed using the corresponding radiometric coefficients for each band. FLAASH, a module in ENVI software, was used for atmospheric correction. Geometric correction was applied to eliminate geometric distortions. For Hyperion data, in addition to the above processes, the following steps were performed due to water vapor and noise influence, bad lines, and striping: (1) Ninety-three bands were identified as invalid or useless and were removed, resulting in 149 retained bands. (2) Bad lines were repaired using the average value of neighbor lines. (3) A global destriping

method was employed to reduce striping artifacts [44–47]. The preprocessed results of ZY-1 02D AHSI data and Hyperion data are shown in Figure 5.

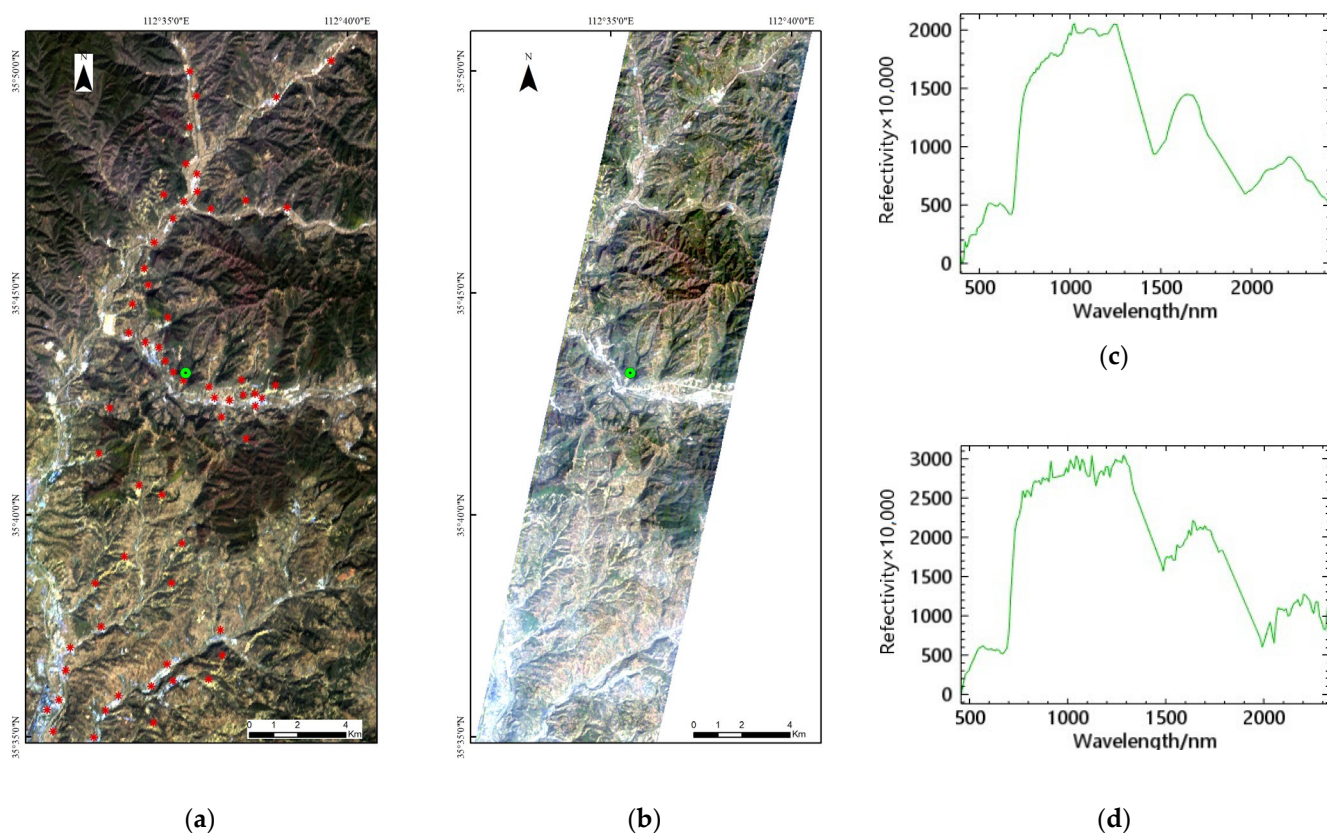


Figure 5. Preprocessed results. (a) Results of ZY-1 02D AHSI data, with a B29 (R), B19 (G), B10 (B) true color composite image. The red points represent field samples, and the green point indicates the position of the vegetation spectrum. (b) Results of Hyperion data, with a B29 (R), B20 (G), B12 (B) true color composite image. The green point indicates the position of the vegetation spectrum. (c) Vegetation spectrum of ZY-1 02D image at the green point. (d) Vegetation spectrum of Hyperion image at the green point.

3.3. Extraction Method of Alteration Minerals

Currently, three main methods are used for extracting hyperspectral mineral information: spectral matching, spectral characteristic parameters, and spectral unmixing [48]. Spectral matching methods include spectral angle mapping (SAM), matching filtering (MF), and mixture-tuned matched filtering (MTMF). Representative methods of spectral characteristic parameters include spectral feature fitting (SFF), spectral absorption index (SAI), and absorption band positioning analysis [49,50]. Spectral unmixing involves using linear or nonlinear unmixing methods to determine mineral content [51,52]. However, these methods often fall short of achieving precise mineral identification and suffer from low accuracy. The spectral matching method is not sensitive to tiny differences in mineral spectra, and is easily affected by external interference such as terrain and background, so it cannot highlight the importance of spectral absorption characteristics. Compared with the spectral matching method, the spectral characteristic parameter method enhances the ability of distinguishing ground objects, but in practical application, it is easily affected by spectral signal-to-noise ratio and mineral mixing, and the spectral shape of mineral characteristic absorption is not fully considered. Hence, in order to improve the recognition accuracy of alteration minerals and reduce the influence of other interferences, an integrated extraction method of hyperspectral mineral information that combines spectral feature

matching and diagnostic characteristic parameters is proposed in this study, considering the spectral characteristics of different minerals.

3.3.1. Spectral Feature Matching Method

The spectral matching method plays an important role in the identification and extraction of alteration minerals through comparing the full spectral curve with the reference spectrum. In recent years, spectral feature matching has become more targeted, focusing on subsections of the characteristic spectral curve of different minerals. Different spectral matching methods involve selecting a similarity measure function, which is essential for calculating the matching degree. Examples of similarity measure functions include Euclidean distance, coefficient, and SAM. SAM calculates the spectral angle between the target spectrum and the reference spectrum in an N -dimensional vector space [8]. The formula is as follows:

$$\theta = \arccos \frac{\sum_{i=1}^N xy}{\sqrt{\sum_{i=1}^N (x)^2 \sum_{i=1}^N (y)^2}} \quad (1)$$

where θ is the spectral angle, x is the target spectrum, y is the reference spectrum, and N is the number of bands. A smaller angle indicates higher similarity. The MTMF method combines hybrid modulation and MT on the basis of linear mixing and signal processing [23]. The results of MTMF include the MF score image, which compares every endmember spectrum with every pixel spectrum, and an infeasibility image. One constraint of this method is that the content of each endmember must be positive and sum to 1. The advantages of MTMF are that it does not require background endmember spectra and provides high accuracy of in the extraction of alteration minerals.

Reference spectra typically come from three sources: laboratory-measured spectra in standard spectral libraries, field-measured spectra, and pure pixel spectra extracted from images. Endmember extraction involves identifying pure pixels in the image and comparing them with the spectral library to determine the mineral type. In this study, the following steps are performed using ENVI software: (1) applying minimum noise fraction to reduce dimensionality and remove noise, (2) using pixel purity index to identify pure pixels, (3) employing N -dimensional visualization to display the feature spectra of endmembers, and (4) utilizing spectral analysis to determine the mineral type.

3.3.2. Diagnostic Characteristic Parameters

The full spectral curve can be regarded as the superposition of spectral features caused by different components within an object. Therefore, various local spectral absorption characteristics can be utilized as diagnostic characteristic parameters to identify different minerals. A local absorption feature diagram is shown in Figure 6 [24]. The absorption characteristics of the spectral curve are mainly composed of two reflection points (S1 and S2) and an absorption valley point (M).

In the figure, λ_{S1} , R_{S1} , λ_{S2} , R_{S2} , λ_M , and R_M represent the wavelength and reflectivity of the points (S1, S2, and M). The main diagnostic characteristic parameters include (1) absorption position (λ_M), which is the wavelength of the maximum absorption value of the spectral curve; (2) absorption reflectivity (R_M), which is the reflectivity of the maximum absorption value of the spectral curve; (3) absorption width (W), which is the wavelength width between the two reflection points, S1 and S2; (4) absorption depth (H), which is the distance between the absorption valley point (M) and the connecting line between the two reflection points (S1 and S2), known as the nonabsorbing baseline; (5) absorption area (A), which is the area enclosed by the nonabsorbing baseline and the spectral curve; (6) absorption symmetry (S), which is the ratio of the area on the left side of the adsorption position to the area on the right side, divided by the vertical line of the absorption position.

The continuum removal algorithm is adopted for information extraction to further highlight the diagnostic spectral characteristics of alteration minerals.

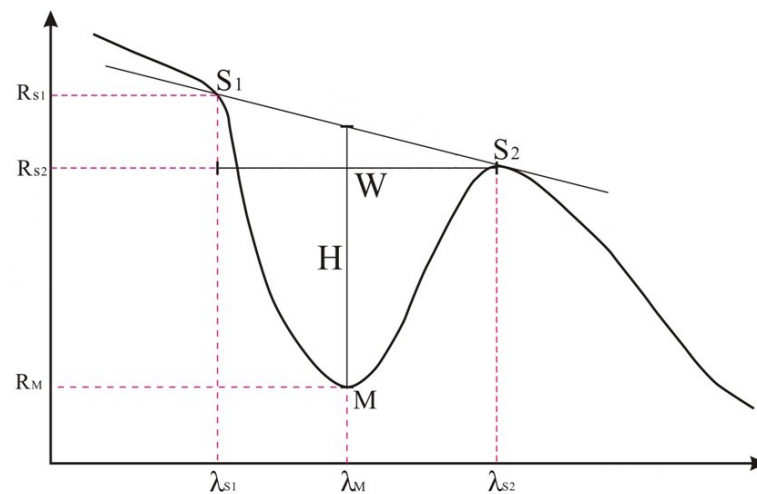


Figure 6. Local absorption feature. S1 and S2 are two reflection points and M is an absorption valley point. λ_{S1} , R_{S1} , λ_{S2} , R_{S2} , λ_M , and R_M are the wavelength and reflectivity of the points (S1, S2, and M), respectively. W is absorption width and H is absorption depth.

3.3.3. Integrated Method of Spectral Feature Matching and Diagnostic Characteristic Parameters

A method of comprehensive spectral features matching and diagnostic characteristic parameters based on mineral hierarchical identification theory was proposed to extract alteration mineral information in the study area. The main steps are as follows. (1) Analyze the position, width, depth, area, and symmetry of the main characteristic absorption based on the spectral characteristics of minerals. (2) Calculate the spectral feature matching degree between the spectral characteristics of different minerals and their corresponding standard spectra. (3) Obtain the main diagnostic characteristic parameters of different minerals. (4) Set threshold values for the above parameters to obtain the distribution of mineral information. The technical flowchart of this study is shown in Figure 7.

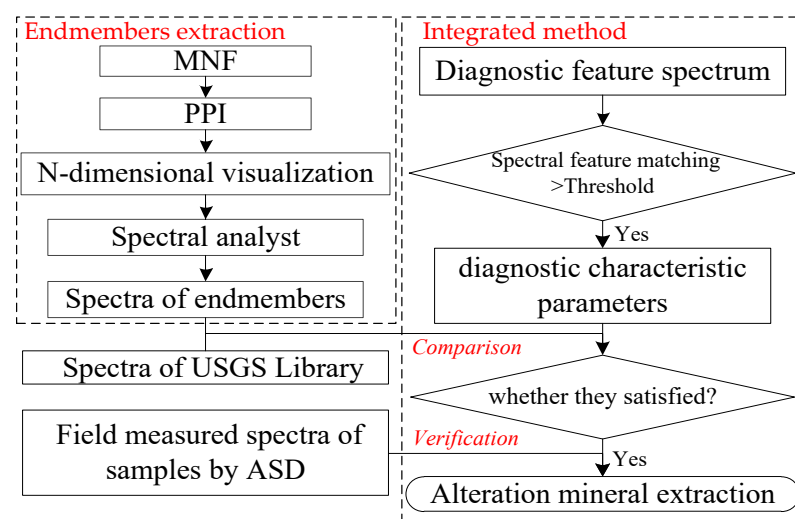


Figure 7. Technical flowchart of integrated method in this research.

3.4. Accuracy Assessment

Sixty field samples collected in the study area (Figure 5a) were used to evaluate the extraction results of alteration minerals based on the XRD analysis and quantitatively

analyze the identification effects. Using the confusion matrix, the extracted results of alternation minerals were compared with the results of XRD analysis to calculate the producer's accuracy (PA), user's accuracy (UA), and overall accuracy (OA) [53–57].

4. Results and Analysis

4.1. Extraction Results of the Diagnostic Characteristic Parameters of Typical Minerals

4.1.1. Clay Mineral

Using the mentioned method of endmember extraction, the endmembers of the clay mineral were obtained from hyperspectral remote sensing imagery, as shown in Figure 8. The continuum removal algorithm was utilized to enhance the diagnostic spectral characteristics of clay minerals [58]. The spectral curve exhibits absorption characteristics of clay minerals at 2200 nm, which are similar to the characteristics of kaolinite and montmorillonite in the spectral library. The diagnostic absorption characteristics were further analyzed through calculating the diagnostic characteristic parameters using the IDL language as shown in Table 4.

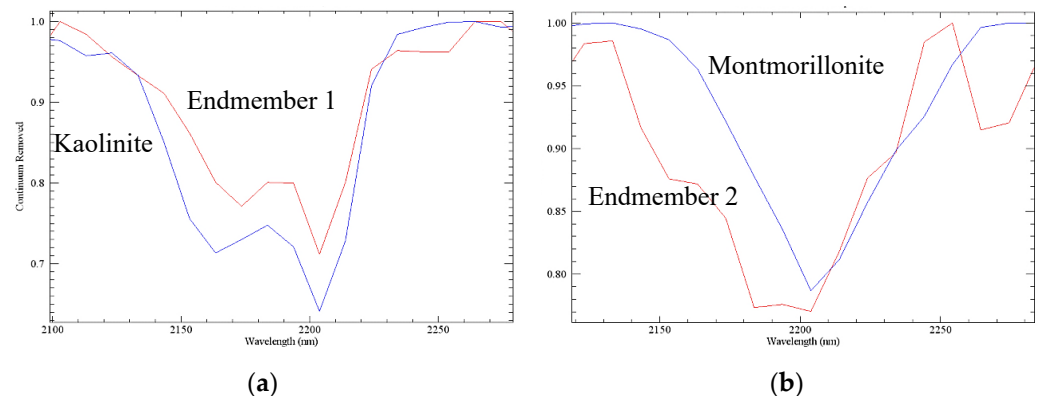


Figure 8. Comparison of the endmember spectra of clay minerals extracted from the hyperspectral imagery and the standard spectra in USGS_MIN spectral library. (a) Endmember 1 and kaolinite; (b) Endmember 2 and montmorillonite.

Table 4. Comparison of diagnostic characteristic parameters of the endmember spectra of clay minerals extracted from the hyperspectral imagery and standard spectra in USGS_MIN spectral library.

Name	λ_M/nm	R_M^1	W/nm	H	A	S
Endmember 1	2203	0.1392	162	0.2882	141.62	1.58
Endmember 2	2203	0.1446	121	0.2297	103.97	1.33
Kaolinite	2203	0.3824	202	0.3589	175.70	2.23
Montmorillonite	2203	0.5230	141	0.2132	128.23	1.02

¹ Except for R_M , which represents the actual reflectance value at the absorption position, the other parameters are calculated after continuum removal.

The quantitative calculation results of the diagnostic characteristic parameters clearly indicate that the spectral absorption position is completely consistent. However, the spectral reflectance of the endmember spectra is slightly low because they are obtained from hyperspectral satellite remote sensing images and affected by atmospheric interference, affecting the absorption depth and area to some extent. However, the difference in absorption width and depth between endmember 2 and montmorillonite, obtained after continuum removal, is only 14.18% and 7.74%, respectively. Therefore, the diagnostic characteristic parameters of the extracted mineral endmember spectra are consistent with the spectra in the spectral library. Specifically, the absorption position, width, and depth of endmember 1 and endmember 2 are consistent with kaolinite and montmorillonite in the spectral library, respectively, allowing for a preliminary identification as clay minerals.

4.1.2. Carbonate Mineral

For carbonate minerals, the classical diagnostic characteristic parameters of the spectral curves mainly occur at 2300 nm, considering the remarkable influence of atmospheric water vapor. Therefore, noise bands at 1400 and 1900 nm in the hyperspectral images were eliminated. After continuum removal, the diagnostic absorption spectral characteristics of the endmembers extracted from the hyperspectral satellite remote sensing image were compared with typical carbonate minerals in the spectral library, as shown in Figure 9. The quantitative analysis results of the diagnostic characteristic parameters of carbonate minerals are shown in Table 5.

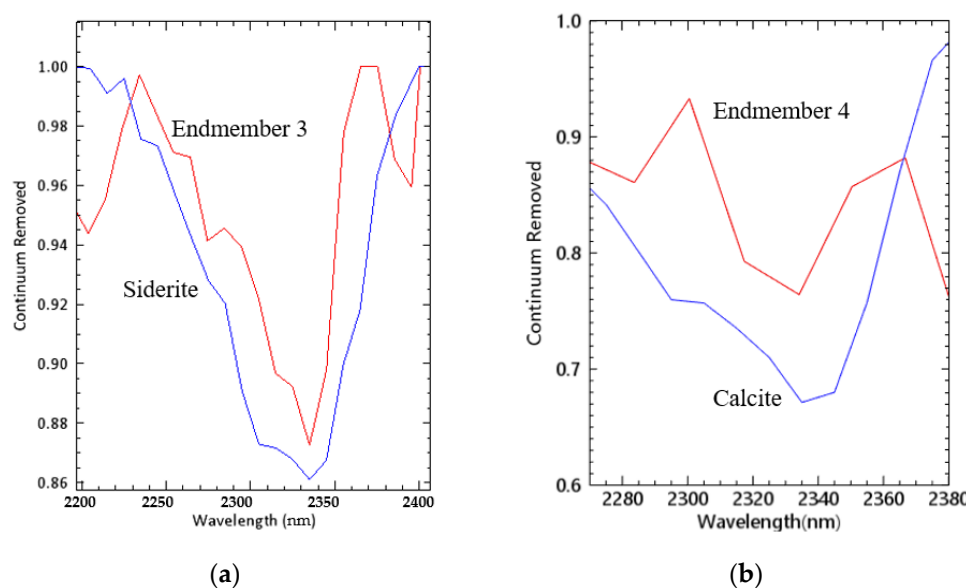


Figure 9. Comparison of the endmember spectra of carbonate minerals extracted from the hyperspectral imagery and the standard spectra in USGS_MIN spectral library. (a) Endmember 3 and siderite; (b) Endmember 4 and calcite.

Table 5. Comparison of diagnostic characteristic parameters of the endmember spectra of carbonate minerals extracted from the hyperspectral imagery and standard spectra in USGS_MIN spectral library.

Name	λ_M/nm	R_M^1	W/nm	H	A	S
Endmember 3	2335	0.2013	131	0.1274	112.19	2.98
Endmember 4	2335	0.5301	101	0.2358	93.68	2.64
Siderite	2335	0.4119	202	0.1390	186.79	2.36
Calcite	2335	0.5718	192	0.3286	161.09	2.92

¹ Except for R_M , which represents the actual reflectance value of the absorption position, the other parameters are calculated after continuum removal.

The results show that the spectral absorption position of the endmember is exactly the same as that of calcite and siderite. However, the reflectivity of the endmember obtained from the hyperspectral imagery is low due to atmospheric interference during image acquisition, resulting in slightly lower absorption depth and absorption area. In particular, the absorption reflectivity of endmember 3 is only 51.13% of that of siderite in the spectral library. The absorption width of the endmember spectrum is narrow, and the absorption area is small overall. However, the absorption depth of endmember 3 is consistent with siderite, with a difference of only 8.34%. The absorption reflectivity and symmetry of endmember 3 are similar to that of calcite, with differences of only 7.29% and 9.59%, respectively. Therefore, the absorption position, depth, and symmetry of the extracted endmember 3 and endmember 4 are consistent with calcite and siderite in the spectral

library, respectively, allowing for a preliminary determination that these endmembers represent carbonate minerals.

4.2. Extraction Results Using the Integrated Method of Spectral Feature Matching and Diagnostic Characteristic Parameters

4.2.1. Clay Minerals

Clay minerals were extracted using the proposed integrated method based on the indications of clay minerals, such as the distinct spectral feature from 2100 nm to 2300 nm and the diagnostic characteristic parameters, including the absorption position, width, and depth at 2203 nm. The spectral feature matching degrees were obtained using the SAM within the 2100–2300 range. The absorption position, width, and depth of pixels with a high matching degree were calculated at 2203 nm. If these thresholds of diagnostic characteristic parameters were met, then the pixels were identified as clay minerals. The distribution of clay minerals in the study area is illustrated in Figure 10, which compares the extraction results from ZY-1 02D data and Hyperion data.

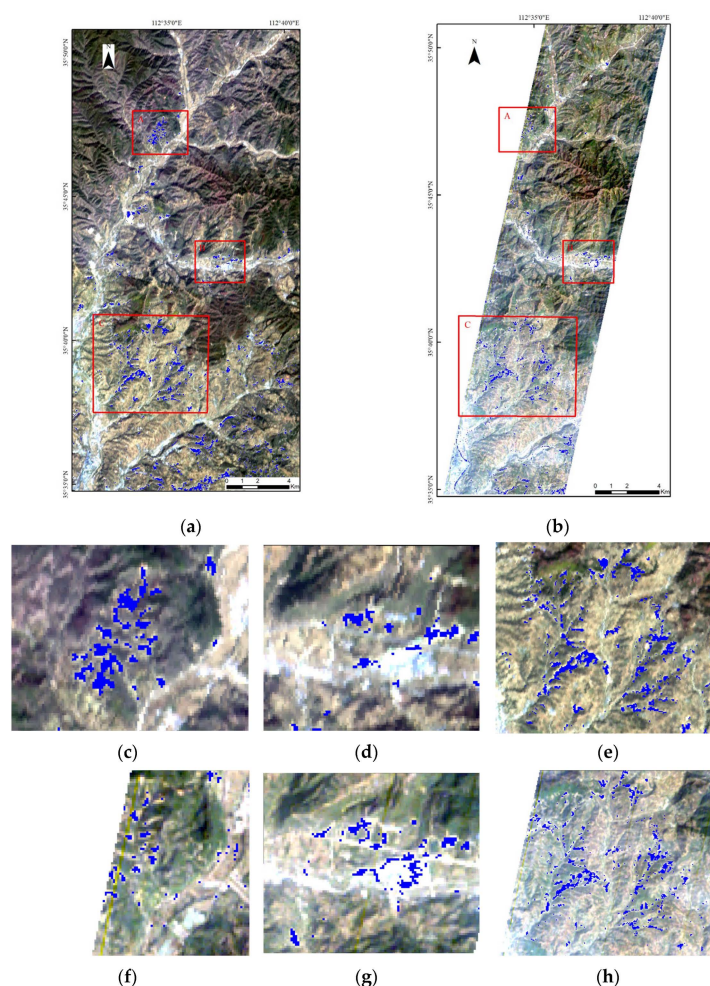


Figure 10. Comparison of the extraction results of clay minerals extracted from ZY-1 02D data and Hyperion data. The distributions of clay minerals are denoted in blue. (a) The extraction result of ZY-1 02D data; (b) The extraction result of Hyperion data; (c–e) The zoom-in detailed subfigures of region A, B, and C of ZY-1 02D data, respectively; (f–h) The zoom-in detailed subfigures of region A, B, and C of Hyperion data, respectively.

As shown in Figure 9, clay minerals are mainly concentrated in the central and southern areas of the study area, with sporadic distribution in the northwest part. Several obvious anomalies can be observed. In accordance with the actual geological data, the

central region of the study area corresponds to the Hudi coal mine area of Qinshui Basin, Jincheng, Shanxi, China, which is consistent with the extraction results of clay minerals. In addition, the distribution of clay minerals is relatively consistent when comparing the extraction results from Hyperion data, with both datasets showing concentrations in the central and southern parts of the study area.

4.2.2. Carbonate Minerals

Using the proposed method, carbonate minerals were identified on the basis of the spectral feature matching degree within the 2200 nm to 2400 nm range and the diagnostic characteristic parameters, including the absorption position, depth, and symmetry at 2335 nm. First, the spectral feature matching degrees were acquired using the MTMF within 2200–2400 nm. Second, the absorption position, depth, and symmetry of pixels with a high matching degree were calculated at 2335 nm. Finally, carbonate minerals were extracted in the study area when the parameters reached the defined thresholds, as shown in Figure 11.

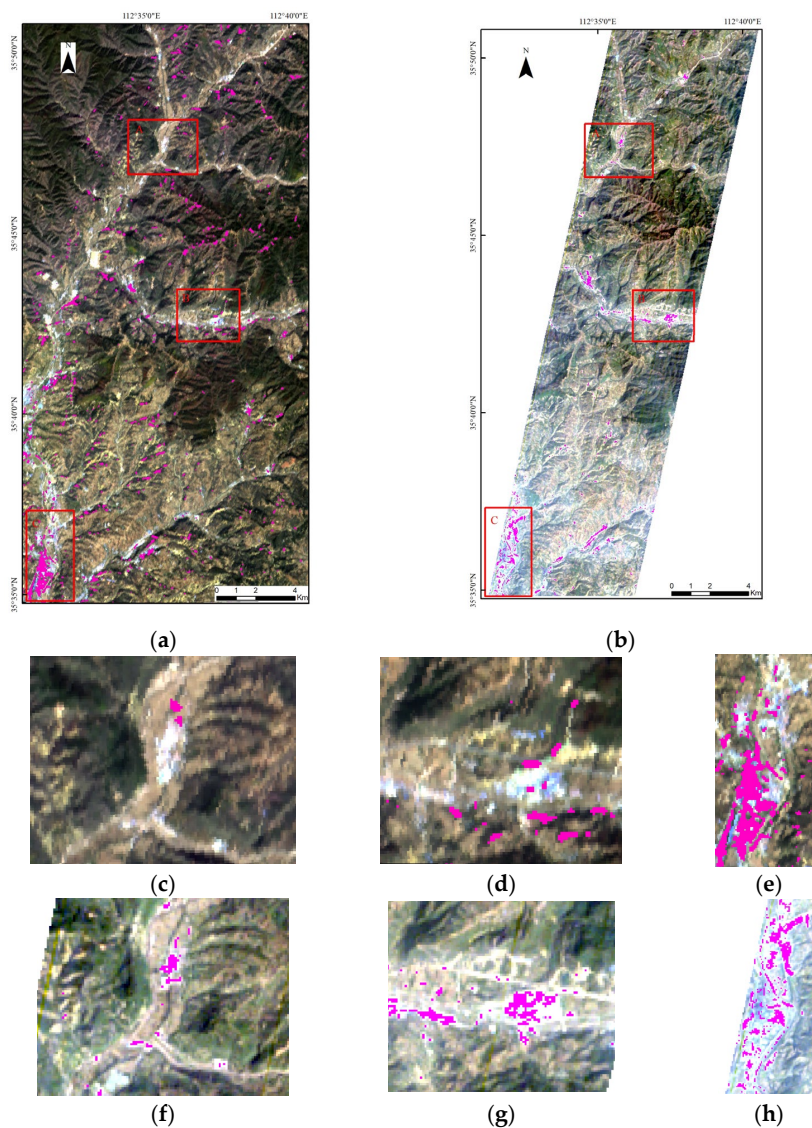


Figure 11. Comparison of the extraction results of carbonate minerals extracted from ZY-1 02D and Hyperion data. The distributions of carbonate minerals are denoted in magenta (a) The extraction result of ZY-1 02D data; (b) The extraction result of Hyperion data; (c–e) The zoom-in detailed subfigures of region A, B, and C of ZY-1 02D data, respectively; (f–h) The zoom-in detailed subfigures of region A, B, and C of Hyperion data, respectively.

Carbonate minerals are widespread in the central and southwest of the study area, with a thin distribution in the northern part. The central region of the study area corresponds to the Hudi coal mine area. However, a large number of anomalies in the southwest have not been effectively verified. Field surveys indicate that no CBM mining has been conducted although coal seams distributed underground exist. Overall, the extraction results of carbonate minerals using ZY-1 02D data are relatively consistent with the results obtained from Hyperion data in the middle and southern parts of the study area.

4.3. Accuracy Assessment

Four evaluation factors, such as PA, UA, and OA, were used to quantitatively analyze the extraction results of alteration minerals from ZY-1 02D and Hyperion data. These factors were compared with the results of XRD analysis, as shown in Table 6.

Table 6. Accuracy assessment of ZY-1 02D and Hyperion data.

Data	Minerals	PA (%)	UA (%)	OA (%)
ZY-1 02D	Clay	81.25	83.87	81.67
	Carbonate	79.41	81.82	79.03
Hyperion	Clay	78.12	80.64	78.33
	Carbonate	73.53	83.33	76.67

The overall accuracy of clay and carbonate mineral extraction results from ZY-1 02D data is 81.67% and 79.03%, respectively, which is better than the Hyperion data (78.33% and 76.67%). However, all accuracy values are greater than 75%, confirming the reliability of alteration mineral extraction using hyperspectral remote sensing technology. Furthermore, the user's accuracy of clay minerals from ZY-1 02D data and carbonate minerals from Hyperion data reached 83.87% and 83.33%, respectively. This further demonstrates that different data have their unique advantages for the extraction of different minerals.

5. Discussion

5.1. Analysis of the Influence of Different Hyperspectral Satellite Remote Sensing Data

In this research, both ZY-1 02D and Hyperion images were used to extract alteration minerals. Although the two datasets have the same spatial resolution and a large number of bands as hyperspectral satellite remote sensing data, several differences are still observed. Hyperion data contain 76 more bands than ZY-1 02D data due to the higher spectral resolution of SWIR bands in Hyperion data (10 nm) compared with ZY-1 02D data (20 nm) [59]. This results in Hyperion data having more spectral details but also containing a larger amount of redundant information. For example, although the vegetation spectral curves at the same location exhibit a similar waveform, the SWIR bands of Hyperion data may exhibit slight fluctuations, which can be either a spectral characteristic or noise, as shown in Figure 5c,d. In addition, the reflectivity of Hyperion data is universally higher than ZY-1 02D data, making the Hyperion images appear brighter (Figure 12). However, the advantage of ZY-1 02D data is their 60 km width, allowing for large-scale observation. Furthermore, the Hyperion data may contain bad lines and striping due to detector element malfunctions and systematic noise, which can affect the extraction results.

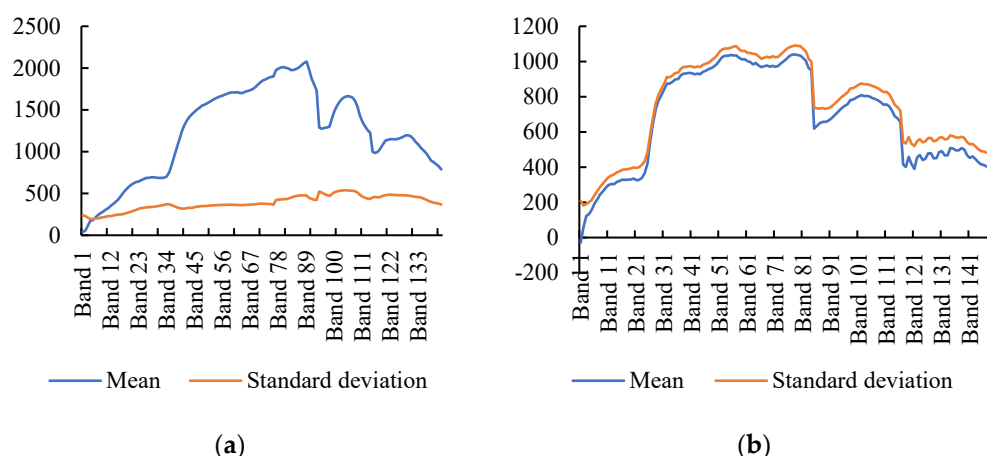


Figure 12. Data quality comparison of the ZY-1 02D (a) and Hyperion (b) images.

5.2. Analysis of Extraction Efficiency of Different Alteration Minerals

The normalized difference vegetation index was utilized to eliminate vegetation and reduce its influence on alteration mineral extraction. The extraction results of clay and carbonate minerals from the ZY-1 02D and Hyperion images were obtained in the bare areas of the study area using an integrated method of spectral feature matching and diagnostic characteristic parameters. The alteration minerals were predominantly distributed in the central and southern regions. On the basis of the regional geology, seismic data, and well logging information in the study area, the central region was identified as the Jincheng Hudi mine area of the Qinshui Basin [60]. The distribution of clay and carbonate minerals was consistent between the two different hyperspectral imageries in the middle of the study area. However, clay minerals still exhibited distribution in the northwest part of the study area, with several obvious anomalies in the ZY-1 02D image. They cannot be extracted in the Hyperion data due to the narrower width. Apparent false anomalies were observed along the river in the southwest of the Hyperion image. For the carbonate minerals, a large number of anomalies existed in the southwestern part of the study area, but they had not been effectively verified. Although coal seams were indeed distributed based on field surveys, CBM was not being extracted.

Quantitative assessment of the extraction results showed that the PA, UA, and OA of clay minerals extracted using ZY-1 02D data were higher than those obtained from Hyperion data. Specifically, the OA was 3.34% higher. Except for the UA of carbonate minerals extracted using ZY-1 02D data, which was 1.51% lower, the other factors were higher than Hyperion data. Overall, the extraction efficiency of ZY-1 02D data was better than that of Hyperion data for the two different minerals. In terms of different minerals, the extraction efficiency of clay minerals was better than that of carbonate minerals. This difference can be attributed to the spectral characteristics of carbonate minerals falling between 2200 and 2400 nm, where the data quality of these bands is poorer compared with the range from 2100 nm to 2300 nm, which severely limits the quality of the extraction results.

However, the extraction results of alteration minerals are highly affected by other interfering factors, such as fertilizer, acid rain, and chemical pollution, due to the feeble and imperceptible nature of the alteration minerals caused by CBM microseepage. Moreover, distributions of alteration minerals many not necessarily correlate the regions of CBM enrichment because microseepage can be controlled using drainage and structure [61]. Thus, the mineral alterations in this study area were only caused by CBM microseepage to the ground surface. Further experiments are required to investigate the spectral characteristics of alteration minerals in more CBM enrichment areas [62].

Consequently, some works should be studied in the future. First, the analysis and comparison of spectra from a larger number of field samples should be conducted. Second, further fieldwork is necessary to verify the universality and generalizability of this method in other regions. Specifically, geochemical analysis is required in the future to investigate

the alteration minerals caused by CBM hydrocarbon microseepage. Finally, the study did not involve the extraction of altered vegetation due to the immaturity of extraction methods. The diagnostic spectral features of altered vegetation should be explored in future research. Therefore, additional investigation into the potential geological application of hyperspectral data is crucial and promising.

6. Conclusions

In this study, alteration minerals were successfully extracted from civilian ZY-1 02D hyperspectral data and Hyperion data in the Hudi coal mine area of the Qinshui Basin. A mineral identification method that combines spectral feature matching and diagnostic characteristic parameters was adopted on the basis of the spectral characteristics of clay minerals and carbonate minerals. The extraction results of ZY-1 02D and Hyperion data were compared with geological data to effectively extract alteration minerals in CBM enrichment areas. This research demonstrates the application potential of domestic hyperspectral data in CBM identification and provides valuable technical support for large-scale and rapid CBM exploration.

The following conclusions were obtained:

- (1) The extraction of alteration minerals, including clay and carbonate minerals, was successfully achieved using ZY-1 02D and Hyperion data. The distribution of clay and carbonate minerals exhibited good accuracy (81.67% and 79.03%, respectively) when analyzed using XRD.
- (2) Comparing the extraction results of Hyperion data and ZY-1 02D data, the PA, UA, and OA for clay mineral extraction were higher with ZY-1 02D data than with Hyperion data. However, the UA for carbonate mineral extraction using ZY-1 02D data was 1.51% lower than with Hyperion data.
- (3) The study illustrated the potential geological application of hyperspectral satellite remote sensing data in identifying CBM enrichment regions. This method offers a large-scale, convenient, and highly efficient approach compared with traditional seismic exploration and drilling methods.

Author Contributions: Conceptualization, L.C. and X.S.; methodology, L.C.; software, L.C.; validation, L.C., H.C. (Hong Chen) and Y.L.; formal analysis, L.C.; investigation, X.S.; resources, H.C. (Hong Chen); data curation, X.Z.; writing—original draft preparation, L.C.; writing—review and editing, L.C.; visualization, H.C. (Haomin Chen); supervision, X.Z.; project administration, R.L.; funding acquisition, R.L. All authors have read and agreed to the published version of the manuscript.

Funding: This research was funded by the General Program of the National Natural Science Foundation of China, grant number 42271408.

Acknowledgments: ZY-102D AHSI imagery was obtained from China Aero Geophysical Survey and Remote Sensing Center for Natural Resources, and XRD data were measured by Beijing Research Institute of Uranium Geology. We express our sincere thanks. We are also grateful to the USGS Earth Explorer (<https://earthexplorer.usgs.gov/> accessed on 25 October 2019) for providing Hyperion data. Thanks also go to editors and the anonymous reviewers for helping us to improve the quality of the manuscript.

Conflicts of Interest: The authors declare no conflict of interest.

References

1. Moore, T.A. Coalbed methane: A review. *Int. J. Coal Geol.* **2012**, *101*, 36–81. [[CrossRef](#)]
2. Fu, X.; Qin, Y.; Wang, G.G.X.; Rudolph, V. Evaluation of gas content of coalbed methane reservoirs with the aid of geophysical logging technology. *Fuel* **2009**, *88*, 2269–2277. [[CrossRef](#)]
3. Zhang, C.Y.; Qin, Q.M.; Chen, L.; Nan, W.; Zhao, S.S.; Hui, J. Rapid determination of coalbed methane exploration target region utilizing hyperspectral remote sensing. *Int. J. Coal Geol.* **2015**, *150–151*, 19–34. [[CrossRef](#)]
4. Song, X.; Ma, H.; Saalidong, B.M.; Li, K. Petrography, Mineralogy, and Geochemistry of Thermally Altered Coal in the Tashan Coal Mine, Datong Coalfield, China. *Minerals* **2021**, *11*, 1024. [[CrossRef](#)]

5. Gan, F.P.; Dong, X.F.; Yan, B.K.; Liang, S.N. Research progress of spectrometry geological remote sensing. *J. Nanjing Univ. Inf. Sci. Technol. Nat. Sci. Ed.* **2018**, *10*, 44–62. [[CrossRef](#)]
6. Zheng, X.W.; Peng, B.; Shang, K. Assessment of the interpretation ability of domestic satellites in geological remote sensing. *Remote Sens. Nat. Resour.* **2021**, *33*, 1–10. [[CrossRef](#)]
7. Yao, F.; Xu, X.; Yang, J.; Geng, X. A Remote-Sensing-Based alteration zonation model of the Duolong Porphyry Copper Ore District, Tibet. *Remote Sens.* **2021**, *13*, 5073. [[CrossRef](#)]
8. Maghsoudi Moud, F.; van Ruitenbeek, F.; Hewson, R.; van der Meijde, M. An approach to accuracy assessment of ASTER derived mineral maps. *Remote Sens.* **2021**, *13*, 2499. [[CrossRef](#)]
9. Chen, L.; Qin, Q.M.; Chen, C.; Jiang, H.B. Remote sensing information of mineralizing alteration extraction methods. In Proceedings of the 2012 IEEE International Geoscience and Remote Sensing Symposium, Munich, Germany, 22–27 July 2012; pp. 5947–5950. [[CrossRef](#)]
10. Chen, C.; Liang, J.; Yang, G.; Sun, W. Spatio-temporal distribution of harmful algal blooms and their correlations with marine hydrological elements in offshore areas, China. *Ocean. Coast. Manag.* **2023**, *238*, 106554. [[CrossRef](#)]
11. Chen, C.; Chen, Y.; Jin, H.; Chen, L.; Liu, Z.; Sun, H.; Hong, J.; Wang, H.; Fang, S.; Zhang, X. 3D model construction and ecological environment investigation on a regional scale using UAV remote sensing. *Intell. Autom. Soft Comput.* **2023**, *37*, 1655–1672. [[CrossRef](#)]
12. van der Meer, F.D.; van der Werff, H.M.A.; van Ruitenbeek, F.J.A.; Hecker, C.A.; Bakker, W.H.; Noomen, M.F.; Meijde, M.V.D.; Carranza, E.J.M.; de Smeth, J.B.; Woldai, T. Multi- and hyperspectral geologic remote sensing: A review. *Int. J. Appl. Earth Obs. Geoinf.* **2012**, *14*, 112–128. [[CrossRef](#)]
13. Mohamed, A.; Emam, A.; Zoheir, B. SAM-HIT: A simulated annealing multispectral to hyperspectral imagery data transformation. *Remote Sens.* **2023**, *15*, 1154. [[CrossRef](#)]
14. Islam, M.R.; Siddiqa, A.; Ibn Afjal, M.; Uddin, M.P.; Ulhaq, A. Hyperspectral image classification via information theoretic dimension reduction. *Remote Sens.* **2023**, *15*, 1147. [[CrossRef](#)]
15. Zhou, Z.L.; Wang, Y.L.; Wu, Q.M.J.; Yang, C.N.; Sun, X.M. Effective and efficient global context verification for image copy detection. *IEEE Trans. Inf. Forensics Secur.* **2017**, *12*, 48–63. [[CrossRef](#)]
16. Boubanga-Tombet, S.; Huot, A.; Vitins, I.; Heuberger, S.; Veuve, C.; Eisele, A.; Hewson, R.; Guyot, E.; Marcotte, F.; Chamberland, M. Thermal Infrared hyperspectral imaging for mineralogy mapping of a mine face. *Remote Sens.* **2018**, *10*, 1518. [[CrossRef](#)]
17. Yan, B.K.; Dong, X.F.; Wang, Z.; Yang, S.M.; Yu, J.C.; Li, N.; Gan, F.P. Mineral information extraction technology by airborne hyperspectral remote sensing and its application progress: An example of mineralization belts of western China. *Geol. Surv. China* **2016**, *3*, 55–62.
18. Ren, Z.; Zhai, Q.; Sun, L. A novel method for hyperspectral mineral mapping based on clustering-matching and nonnegative matrix factorization. *Remote Sens.* **2022**, *14*, 1042. [[CrossRef](#)]
19. Ye, B.; Tian, S.F.; Cheng, Q.M.; Ge, Y.Z. Application of lithological mapping based on advanced hyperspectral imager (AHSI) imagery onboard Gaofen-5 (GF-5) satellite. *Remote Sens.* **2020**, *12*, 3990. [[CrossRef](#)]
20. Xu, D.X.; Yang, B.; Shao, Z.G.; Liu, C.F.; Wang, D.; Wang, J.P. A hyperspectral analysis of alteration zoning in the Hadamengou gold deposit and its significance for ore prospecting. *Remote Sens. Nat. Resour.* **2023**, *35*, 123–131. [[CrossRef](#)]
21. Yang, X.; Chen, J.G.; Chen, Z.J. Classification of alteration zones based on drill core hyperspectral data using semi-supervised adversarial autoencoder: A case study in Pulang Porphyry Copper Deposit, China. *Remote Sens.* **2023**, *15*, 1059. [[CrossRef](#)]
22. Wang, Q.; Ren, G.L. Application of hyperspectral remote sensing data-based anomaly extraction in copper-gold prospecting in the Solake area in the Altyn metallogenic belt, Xinjiang. *Remote Sens. Nat. Resour.* **2022**, *34*, 277–285.
23. Chen, Q.; Zhao, Z.; Zhou, J.; Zhu, R.; Xia, J.; Sun, T.; Zhao, X.; Chao, J. ASTER and GF-5 satellite data for mapping hydrothermal alteration minerals in the Longtoushan Pb-Zn Deposit, SW China. *Remote Sens.* **2022**, *14*, 1253. [[CrossRef](#)]
24. Huo, H.Y.; Ni, Z.Y.; Jiang, X.G.; Zhou, P.; Liu, L. Mineral mapping and ore prospecting with HyMap data over Eastern Tien Shan, Xinjiang Uyghur Autonomous Region. *Remote Sens.* **2014**, *6*, 11829–11851. [[CrossRef](#)]
25. Molan, Y.E.; Refahi, D.; Tarashti, A.H. Mineral mapping in the Maherabad area, eastern Iran, using the HyMap remote sensing data. *Int. J. Appl. Earth Obs. Geoinf.* **2014**, *27*, 117–127. [[CrossRef](#)]
26. Dong, X.F.; Gan, F.P.; Li, N.; Yan, B.K.; Zhang, L.; Zhao, J.Q.; Yu, J.C.; Liu, R.Y.; Ma, Y.N. Fine mineral identification of GF-5 hyperspectral image. *J. Remote Sens.* **2020**, *24*, 454–464. [[CrossRef](#)]
27. Pour, A.B.; Zoheir, B.; Pradhan, B.; Hashim, M. Editorial for the special issue: Multispectral and hyperspectral remote sensing data for mineral exploration and environmental monitoring of mined areas. *Remote Sens.* **2021**, *13*, 519. [[CrossRef](#)]
28. Tan, W.; Wang, S.; He, H.; Qi, W. Reconstructing coastal blue with blue spectrum based on ZY-1 (02D) satellite. *Optik* **2021**, *242*, 166901.
29. Tian, J.; Su, S.; Tian, Q.; Zhan, W.; Xi, Y.; Wang, N. A novel spectral index for estimating fractional cover of non-photosynthetic vegetation using near-infrared bands of Sentinel satellite. *Int. J. Appl. Earth Obs. Geoinf.* **2021**, *101*, 102361. [[CrossRef](#)]
30. Zhong, Y.; Wang, X.; Wang, S.; Zhang, L. Advances in spaceborne hyperspectral remote sensing in China. *Geo Spat. Inform. Sci.* **2021**, *24*, 95–120.
31. Sun, W.; Liu, K.; Ren, G.; Liu, W.; Yang, G.; Meng, X.; Peng, J. A simple and effective spectral-spatial method for mapping large-scale coastal wetlands using China ZY1-02D satellite hyperspectral images. *Int. J. Appl. Earth Obs. Geoinf.* **2021**, *104*, 102572. [[CrossRef](#)]

32. Li, G.J.; Yang, X.S.; Zhang, X.; Li, X.M.; Li, D.L.; Du, C. Application and analysis of ZY1-02D hyperspectral data in geological and mineral survey. *Remote Sens. Land Resour.* **2021**, *33*, 134–140. [[CrossRef](#)]
33. Sun, Y.; Liu, J.J.; Zhai, D.G.; Liu, Z.J.; Zhang, F.F.; Zhao, Y.J.; Liu, P.F.; Wang, Z.T. Alteration minerals mapping and identification of gold mineralization belt based on ZY1-02D hyperspectral data in Fangshankounanshan area, Gansu Province. *Geol. Explor.* **2022**, *58*, 399–409. [[CrossRef](#)]
34. Farooq, S.; Govil, H. Mapping Regolith and Gossan for mineral exploration in the Eastern Kumaon Himalaya, India using Hyperion data and object oriented image classification. *Adv. Space Res.* **2014**, *53*, 1676–1685. [[CrossRef](#)]
35. Liu, L.; Zhou, J.; Han, L.; Xu, X.L. Mineral mapping and ore prospecting using Landsat TM and Hyperion data, Wushitala, Xinjiang, northwestern China. *Ore Geol. Rev.* **2017**, *81*, 280–295. [[CrossRef](#)]
36. Chen, L.; Yang, X.C.; Zhen, G.W. Potential of Sentinel-2 data for alteration extraction in coal-bed methane reservoirs. *Ore Geol. Rev.* **2019**, *108*, 134–146. [[CrossRef](#)]
37. Wang, N.; Qin, Q.M.; Chen, L.; Bai, Y.B.; Zhao, S.S. Dynamic monitoring of coalbed methane reservoirs using Super-Low Frequency electromagnetic prospecting. *Int. J. Coal Geol.* **2014**, *127*, 24–41. [[CrossRef](#)]
38. Pashin, J.C.; Mcintyre-Redden, M.R.; Mann, S.D.; Kopaska-Merkel, D.C.; Varonka, M.; Orem, W. Relationships between water and gas chemistry in mature coalbed methane reservoirs of the Black Warrior Basin. *Int. J. Coal Geol.* **2014**, *126*, 92–105. [[CrossRef](#)]
39. Noomen, M.F.; van der Werff, H.M.A.; van der Meer, F.D. Spectral and spatial indicators of botanical changes caused by long-term hydrocarbon seepage. *Ecol. Inf.* **2012**, *8*, 55–64. [[CrossRef](#)]
40. van der Meer, F.D.; van Dijk, P.V.; van der Werff, H.M.A.; Yang, H. Remote sensing and petroleum seepage: A review and case study. *Terra Nova* **2002**, *14*, 1–17. [[CrossRef](#)]
41. Hunt, G.R.; Ashley, R.P. Altered rock spectra in the visible and near infrared. *Econ. Geol.* **1979**, *74*, 1613–1629. [[CrossRef](#)]
42. Kühn, F.; Oppermann, K.; Horig, B. Hydrocarbon index—An algorithm for hyperspectral detection of hydrocarbons. *Int. J. Remote Sens.* **2004**, *25*, 2467–2473. [[CrossRef](#)]
43. Cun, C.L.; Zhang, H.W.; Fan, S.T.; Li, Y.F.; Yun, X.D. Atmospheric correction and application of ZY1-02D hyperspectral data. *Remote Sens. Inf.* **2022**, *37*, 45–50.
44. Chen, S.B.; Chen, L.; Liu, Y.L.; Li, X.L. Experimental simulation on mixed spectra of leaves and calcite for inversion of carbonate minerals from EO-1 Hyperion data. *GISci. Remote Sens.* **2013**, *50*, 690–703. [[CrossRef](#)]
45. Bhattacharya, S.; Majumdar, T.J.; Rajawat, A.S.; Panigrahy, M.K.; Das, P.R. Utilization of Hyperion data over Dongargarh, India, for mapping altered/weathered and clay minerals along with field spectral measurements. *Int. J. Remote Sens.* **2012**, *33*, 5438–5450. [[CrossRef](#)]
46. Gersman, R.; Ben Dor, E.; Beyth, M.; Avigad, D.; Abraha, M.; Kibreab, A. Mapping of hydrothermally altered rocks by the EO-1 Hyperion sensor, Northern Danakil Depression, Eritrea. *Int. J. Remote Sens.* **2008**, *29*, 3911–3936. [[CrossRef](#)]
47. Kruse, F.A.; Boardman, J.W.; Huntington, J.F. Comparison of airborne hyperspectral data and EO-1 Hyperion for mineral mapping. *IEEE Trans. Geosci. Remote Sens.* **2003**, *41*, 1388–1400. [[CrossRef](#)]
48. Li, N.; Dong, X.F.; Gan, F.P.; Yan, B.K. Application evaluation of ZY1-02D satellite hyperspectral data in geological survey. *Spacecr. Eng.* **2020**, *29*, 186–191. [[CrossRef](#)]
49. Zaini, N.; van der Meer, F.; van der Werff, H. Effect of grain size and mineral mixing on carbonate absorption features in the SWIR and TIR wavelength regions. *Remote Sens.* **2012**, *4*, 987–1003. [[CrossRef](#)]
50. Li, H.S.; Zhou, P.; Han, M.X.; Huo, H.Y.; Cui, Y.M.; Geng, L.P. Research and development of mineral recognition software module based on spectral absorption index. *Comput. Mod.* **2012**, *198*, 69–72. [[CrossRef](#)]
51. Chen, X.L. Research on Emission Spectral Feature Extraction of Typical Mineral and Rock Spectral Unmixing. Ph.D. Thesis, Northeastern University, Shenyang, China, 2013.
52. Sun, X.; Xu, L.L.; Wang, X.Y.; Tian, Y.; Wang, W.; Zhang, Z.Y. Mineral identification from hyperspectral images based on the optimized K-P-Means unmixing method. *Remote Sens. Nat. Resour.* **2022**, *34*, 43–49. [[CrossRef](#)]
53. Yang, X.C.; Chen, L. Evaluation of automated urban surface water extraction from Sentinel-2A imagery using different water indices. *J. Appl. Remote Sens.* **2017**, *11*, 026016. [[CrossRef](#)]
54. Chen, C.; Liang, J.; Xie, F.; Hu, Z.; Sun, W.; Yang, G.; Yu, J.; Chen, L.; Wang, L.H.; Wang, L.Y.; et al. Temporal and spatial variation of coastline using remote sensing images for Zhoushan archipelago, China. *Int. J. Appl. Earth Obs. Geoinf.* **2022**, *107*, 102711. [[CrossRef](#)]
55. Chen, C.; Fu, J.; Zhang, S.; Zhao, X. Coastline information extraction based on the tasseled cap transformation of Landsat-8 OLI images. *Estuar. Coast. Shelf Sci.* **2019**, *217*, 281–291. [[CrossRef](#)]
56. Liang, J.; Chen, C.; Song, Y.; Sun, W.; Yang, G. Long-term mapping of land use and cover changes using Landsat images on the Google Earth Engine Cloud Platform in bay area—A case study of Hangzhou Bay, China. *Sustain. Horiz.* **2023**, *7*, 100061. [[CrossRef](#)]
57. Chen, H.; Chen, C.; Zhang, Z.; Lu, C.; Wang, L.; He, X.; Chu, Y.; Chen, J. Changes of the spatial and temporal characteristics of land-use landscape patterns using multi-temporal Landsat satellite data: A case study of Zhoushan Island, China. *Ocean Coast. Manag.* **2021**, *213*, 1005842. [[CrossRef](#)]
58. Malenovský, Z.; Homolová, L.; Zurita-Milla, R.; Lukeš, P.; Kaplan, V.; Hanuš, J.; Gastellu-Etchegorry, J.P.; Schaepman, M.E. Retrieval of spruce leaf chlorophyll content from airborne image data using continuum removal and radiative transfer. *Remote Sens. Environ.* **2013**, *131*, 85–102. [[CrossRef](#)]

59. Sun, P.Y.; Ke, Y.H.; Zhong, R.F.; Zhao, S.H.; Liu, Y. Radiance quality assessment of ZY-1-02D VNIC/AHSI image data. *Remote Sens. Technol. Appl.* **2022**, *37*, 938–952.
60. Chen, L.; Li, W.; Chen, L.; Wang, M.F.; Jia, W.J. Potential prediction of coalbed methane anomaly region utilizing Landsat8 OLI and GF-2 images. In Proceedings of the 2019 IEEE International Geoscience and Remote Sensing Symposium, Yokohama, Japan, 28 July 2019; pp. 6819–6822. [[CrossRef](#)]
61. Qin, Q.M.; Zhang, Z.; Chen, L.; Wang, N.; Zhang, C. Oil and gas reservoir exploration based on hyperspectral remote sensing and super-low-frequency electromagnetic detection. *J. Appl. Remote Sens.* **2016**, *10*, 016017. [[CrossRef](#)]
62. Zhen, G.W.; Chen, L.; Chen, C.; Guo, B. Alteration anomaly information extraction using hyperspectral remote sensing in coalbed methane enrichment. In Proceedings of the 2016 IEEE International Geoscience and Remote Sensing Symposium, Beijing, China, 10 July 2016; pp. 5394–5397. [[CrossRef](#)]

Disclaimer/Publisher’s Note: The statements, opinions and data contained in all publications are solely those of the individual author(s) and contributor(s) and not of MDPI and/or the editor(s). MDPI and/or the editor(s) disclaim responsibility for any injury to people or property resulting from any ideas, methods, instructions or products referred to in the content.